Tape-Free, Digital Wearable Band for Exercise Sweat Rate Monitoring

*Manik Dautta, Luis Fernando Ayala-Cardona, Noelle Davis, Ashwin Aggarwal, Jonghwa Park, Shu Wang, Liam Gillan, Elina Jansson, Mikko Hietala, Hyunhyub Ko, Jussi Hiltunen, and Ali Javey**

Monitoring sweat secretion rate is essential for uncovering underlying physical conditions like hyperhidrosis, mental stress, and neural disorders. Often, flexible microfluidic sweat rate monitoring devices use tape as a means of attachment to the skin to tightly seal the collection area. While these single-use, adhesive-backed devices have lightweight and thin interfaces for mounting on the skin, their form factor complicates their potential integration with available commercial wearables, such as smartwatches. Here, a tape-free device, consisting of a 3D-printed sweat collector with a concave surface that is strapped onto the skin to form an effective seal, is presented. The materials, structure, and dimensions of the sweat collector are optimized for conformal device-to-skin contact and efficient capture of sweat. The collector is interfaced with a fluidic microchannel with embedded electrodes for continuous digital monitoring of sweat rate. Long-term exercise-induced local sweat rate from multiple body locations in both multi-subject and longitudinal studies is measured, depicting the correlation between the measured sweat profile and total body fluid loss. The simple installation procedure and reusability of this tape-free device make it a good candidate for integration with the band of a watch.

1. Introduction

Modern wearable devices offer a robust monitoring platform primarily for physical attributes like motion, heart rate, temperature, and electrodermal activity.[1–7] Sweat rate monitoring presents an additional metric to discover indicators of underlying physical conditions that current devices may be unable to access.[3,8–10] For example, sweat rate is important for the assessment and diagnosis of physical conditions like hyperhidrosis (excessive sweating) and hypohidrosis (lack of sweating) during sedentary or daily activities; it can also be used along with fluid intake quantities to assess the dehydration levels of athletes to maintain proper fluid balance and bodily functions.[11–15] Moreover, monitoring the rate of sweat production enables further analyses, as different sweat rates modulate the concentration of secreted analytes and are thus of critical importance for interpreting analyte concentration measurements.[16–19] Even though monitoring sweat rate has been studied tremendously in the past few years, only a few devices have become commercially available.[20,21] In addition, most of the new concepts are yet to be accepted by the medical field for consistent reliable health monitoring due to the requirements of safe and biocompatible build materials, comfortable geometry and form factor, and accessible and consistent mass production.[22–24]

Traditional methods for monitoring sweat rate such as whole-body washdown and gravimetric pads are done off-body, in specialized settings, and with the intervention of trained

---

M. Dautta, N. Davis, A. Aggarwal, J. Park, A. Javey
Department of Electrical Engineering and Computer Sciences
University of California
Berkeley, CA 94720, USA
E-mail: ajavey@berkeley.edu

M. Dautta, L. F. Ayala-Cardona, N. Davis, A. Aggarwal, J. Park, S. Wang, A. Javey
Berkeley Sensor and Actuator Center
University of California
Berkeley, CA 94720, USA

L. F. Ayala-Cardona
Department of Bioengineering
University of California
Berkeley, CA 94720, USA

N. Davis, J. Park, S. Wang, A. Javey
Materials Sciences Division
Lawrence Berkeley National Laboratory
Berkeley, CA 94720, USA

J. Park, H. Ko
School of Energy and Chemical Engineering
Ulsan National Institute of Science and Technology (UNIST)
Ulsan Metropolitan City 44919, Republic of Korea

S. Wang
Department of Materials Science and Engineering
University of California
Berkeley, CA 94720, USA

L. Gillan
VTT Technical Research Centre of Finland Ltd
Espoo 02150, Finland

E. Jansson, M. Hietala, J. Hiltunen
VTT Technical Research Centre of Finland Ltd
Oulu 90590, Finland

The ORCID identification number(s) for the author(s) of this article can be found under https://doi.org/10.1002/admt.202201187.

DOI: 10.1002/admt.202201187

experts.[25–27] Therefore, health status is not immediately available to the user for corrective measures such as replacing lost fluids with a corresponding intake of water or sports drink. Recently, various approaches have been introduced for real-time continuous sweat rate monitoring to replace traditional methods. Among these, soft microfluidics and absorbent fabric swatches or wicking pads have provided a promising opportunity for in situ sweat rate monitoring due to their conformal contact with the epidermis.[28–31] These devices can be manufactured directly on the adhesive or packaged as a temporary tattoo or patch to be attached directly to the skin. Modern medical-grade tapes are designed to be flexible and biocompatible, while providing a thin lightweight interface with the skin for comfortable wear. We envision future sweat analyzers to incorporate different form factors depending on the application, including standalone skin-adhered patches for single-use, or sensors that can be physically and digitally integrated with existing wearable platforms such as a smartwatch. Regarding the patch form factor, the use of an adhesive is required in order to provide a tight seal with the skin. However, for incorporatiing a sensor with a smartwatch, tape-free and reusable packaging would be highly desirable. With this form factor, the sweat sensor can be implemented with either the watch band or the back of a watch. In addition, there are added benefits of a tape-free device. For example, adhesives might leave some residue on the skin, be uncomfortable for hairy skin, or cause dermal irritation for people with fragile skin, including neonates, infants, and the elderly.[32–34] A leakage-free and smartwatch-compatible form factor is yet to be developed for continuous and reliable monitoring of a user's sweat rate during exercise.

Here, we present a wearable, adhesive-free, smartwatch-compatible sweat-rate sensing device made with simple prototyping techniques by integrating a reusable 3D printed sweat collector with a fluidic layer. The engineered geometry and form factor of the 3D printed sweat collector allows for diversified device placement and versatile incorporation of microfluidics to guide the sweat flow in the channel. To maintain close, non-irritating, and long-lasting device-to-skin contact, the shallow concave undersurface sweat collector is made of Agilus30 Clear, a soft material with low elastic modulus. The smooth, soft, and contoured collection well bulges the skin into a concave surface, preserving a tight seal against the skin that prevents sweat leakage without disrupting the subject's mobility. For physical activity applications, this device can be packaged into the band of existing smartwatches or fitness trackers, providing further versatility in health monitoring applications. The impedimetric sensing scheme enabled by the embedded electrodes in the fluidic channel enables digital real-time measurements of the user's sweat rate. This functionality allowed for a multitude of studies to be conducted, in which a relationship between local sweat rate and total fluid loss was uncovered. We envision this tape-free device as a potential alternative to adhesive-based sweat rate monitoring for specific applications. Continuous access to sweat rate monitoring and the reusability of these devices could lead to a consumer product, either as a standalone wearable device or as a smartwatch integrable device.

2. Results and Discussion

2.1. Tape-Free Wearable Sweat Rate Monitoring Device

The tape-free wearable sweat rate device is designed to measure sweat rate during prolonged exercise. The device is primarily composed of two sections: 1) the sweat collector and 2) the fluidic microchannel. As seen in **Figure 1**a, the sweat collector and the fluidic microchannel are separated by an adhesive layer that permits sweat movement between the two sections via a shared inlet. In order to ensure that the device maintains a healthy watertight interface with the skin's surface in the presence of natural wear and tear, the 3D printed sweat collector is composed of a sturdy housing and a soft collection well. Figure 1c,d illustrates both the cross-section and bottom views of the sweat collector and the connection between the housing and collection well. The housing for the sweat collector is made of hard, nonstretchable digital ABS (RGD515 and RGD531) material that offers a stable plane for the collection well and the microfluidic layers to lay on. The skin-facing sweat collection well, however, is made of a soft, smooth, and hydrophobic material Agilus30 Clear that creates a comfortable seal with the curvilinear skin's surface. The sweat collection well's concave elliptical shape and inner ridge lines allow produced sweat to accumulate from high-pressure edges toward the low-pressure center for optimal sweat entry into the fluidic channel.

The fluidic microchannel section (Figure 1a) consists of three thin layers: capping, fluidic, and electrode layer. The top layer of the fluidic microchannel consists of embedded face-to-face comb-like silver parallel flow rate electrodes that are fabricated using a roll-to-roll (R2R) rotary screen-printing method on a polyethylene terephthalate (PET) substrate.[35,36] R2R printing facilitates high throughput manufacturing for low unit cost and good inter-device uniformity. Then a fluidic channel is defined by a laser-cut double-sided tape (3 M 9965), and a hydrophilic capping layer (3 M 9984) is attached to it to seal and wick the sweat collected at the inlet. The capping layer provides more controlled wetting than only an adhesive layer attached to the sweat collector. These layers are aligned such that sweat can travel freely from the collector to the spiraling fluidic layer, capturing admittance measurements from the electrode layer reliably. The layered design allows for easier manufacturing and device dimension modifications; with the addition of alignment markers on each layer, fabrication overlay errors are held to a minimum, increasing device yield rates and leading to consistent sweat measurements across devices. When sweat begins to accumulate in the collection well, the sweat's hydraulic pressure exceeds the inlet's resistance, pushing it through the interface between the collection well inlet and the fluidic layer. As depicted in Figure 1b, the sweat enters the spiral-shaped microfluidic and contacts the embedded electrodes. As sweat continues to flow toward the fluidic outlet, the spiral electrodes are progressively more in contact with sweat, leading to larger admittance values. By connecting the electrode stems to an LCR meter or a custom board that transmits admittance values to an Android app, the admittance time series can be processed to generate a real-time feed of the device's fill volume and sweat rate.[25] This functionality is the basis for the trials and experiments performed in this study.

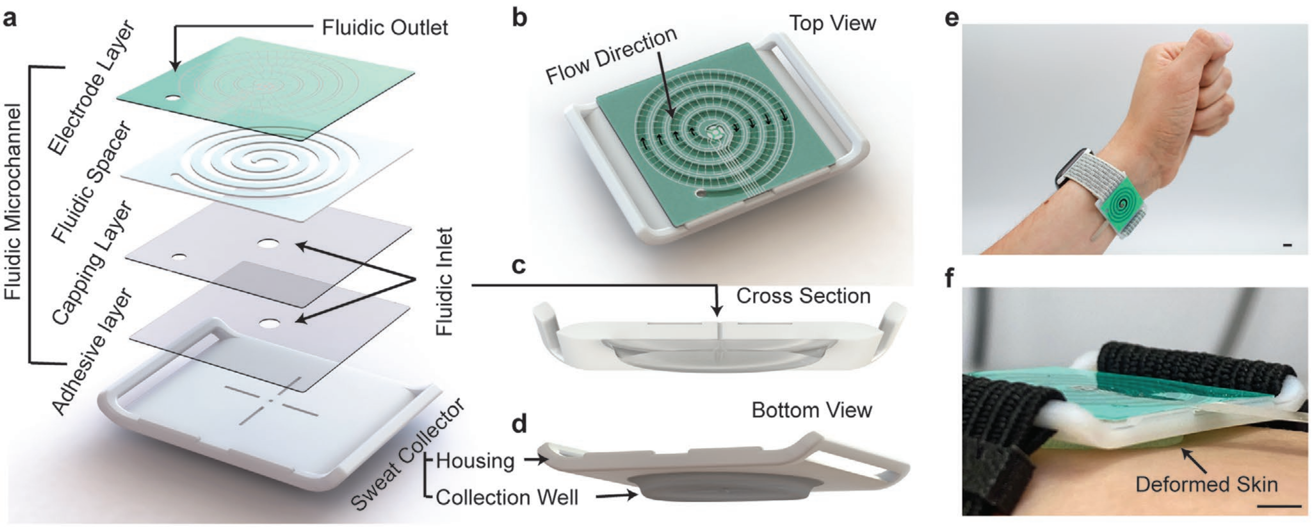

Figure 1. Tape-free 3D printed wearable sweat rate monitoring device. a) Layer-by-layer stack of the device structure including a top electrode layer with a fluidic outlet, a spacer layer defining the fluidic channel, a hydrophilic capping layer with an inlet, and an adhesive layer for attaching the stack to the sweat collector. b) Top view of the device showing the face-to-face comb-like electrode for admittance measurement. c) A cross-sectional view of the sweat collector showing a common fluidic inlet between the soft sweat collector and the hard housing. d) A bottom view of the skin interfacing sweat collection well. e) An optical image of the device mounted on a custom wristband worn by a subject. f) Minimal but essential skin deformation for conformal wearing of the device on the wrist. Scale bar is 1 cm.

The tape-free wearable sweat-sensing device presents a simple, nonintrusive, and accurate method of monitoring secreted sweat levels during prolonged exercise periods without external intervention. As seen in Figure 1e, the sweat sensor can be attached to a commercial smartwatch with a custom band. With similar implementation, the sensor can be attached to the forearm, bicep, ankle, or forehead with ease, without interfering with day-to-day activities.

The close-up view of the sensor's interface with the skin's surface in Figure 1f shows the minimal but essential skin deformation that comfortably seals the collection well on the skin. Combined with its simple manufacturing and assembly process, the sensor's capability to be integrated with commercially available smartwatches lends itself to robust research into the relationships between sweat rate and various health metrics and diseases.

2.2. Optimization of Sweat Collector

Sweat secretion rate depends on the size and distribution of the active sweat glands, which are dependent on the degree of physical activity, body location such as forearm or ankle, and environmental conditions such as temperature and humidity.[12,37–40] For instance, local sweat rate can vary more than 300% between the torso and limbs, with the torso having the highest rate.[14,41] To account for variable sweat rate measurements in multi-subject trials, the collection well needs to be optimized such that the variations in secretion rate from different body locations can be determined. This is achieved by using a collection well with extruded fins, a small curvature that allows no air space, and a large collection well area to cover a sufficient number of activated sweat glands. Further tunability of the sweat rate resolution and volume capacity are discussed in the next section for fluidic microchannel optimization.

As sweat secretion begins, sweat first accumulates under the collection well before it enters the inlet hole that leads into the fluidic channel. This amount of accumulated sweat is referred to as dead volume. As perspiration continues, sweat gland secretory pressure and capillary action push the accumulated sweat from the collection well into the microchannel. Having no curvature in the sweat collector would be ideal, as it decreases the dead volume, which consequently reduces the lag time. **Figure 2**a shows that a flat collection well (curvature distance to bottom = 0 mm) has a very low dead volume (<3 μL) which increases to ≈8 μL if the curvature is 3 mm deep. While no curvature is preferred to reduce the dead volume, a flat collection well makes a very poor seal with the curvilinear skin surface, especially under dynamic conditions. Similarly, it is beneficial for the collection area to be large to maximize the accessible sweat glands. However, a large collection area has a larger dead volume, as sweat first needs to form a globule under the well before flowing into the microchannel shown in Figure 2b. While further tuning is possible, we determined that a 1.14 or 3.432 cm^2 surface area and a 2 mm curvature depth provided an ample seal to the skin with a small lag time for the trials performed in this study.

In addition to the optimization of the design to minimize the dead volume, a good watertight seal is important for a fluidic-based sweat rate device, as otherwise potential leakages from or into the collection area may interfere with the measurements. We have performed two controlled studies to investigate whether our optimized device can provide leakage-free and accurate sweat rate monitoring, as shown in Figure 2c. In Test 1, we placed colored dye on the collection well within the edge and wore it for 6 h. After device removal, a photograph was taken and visually observed that no dye leaked out from the outer mark of the collection well. In Test 2, we made a ≈1 cm hole through the sweat collector, and while the device was

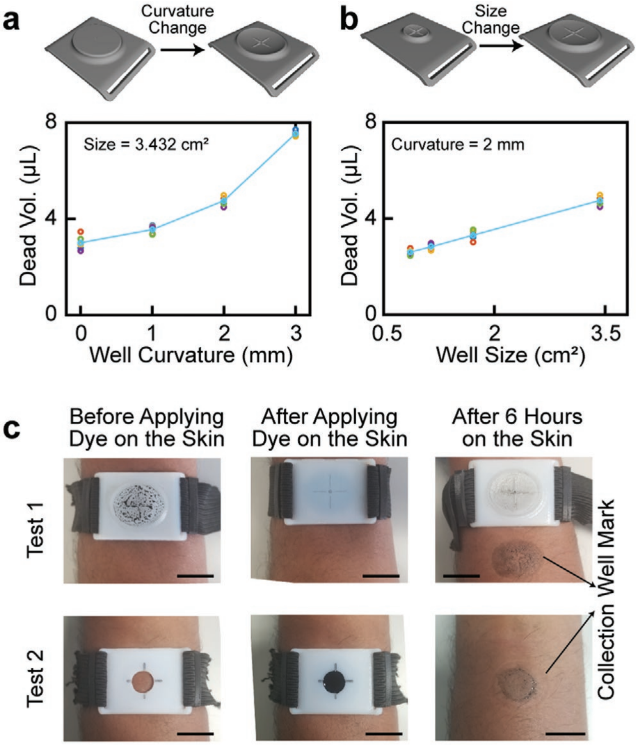

Figure 2. Sweat collector characterization. a,b) Dead volume measurements for varying curvature and size of the collection well. The measurements were repeated five times. c) Optical photographs of the device and skin to show the leakage-free tight seal of the collection well. Colored dye was spotted on the collection well and then placed on the skin for Test 1, while colored dye was directly applied on the skin for Test 2. Scale bar is 2 cm.

worn, the hole was filled with colored dye. When the device was removed after 6 h, the dye was spread into the collection well, but no lateral leakage was found around the collection well mark. These results assert the device's secure seal with the skin and confirm that only sweat produced in the collection well can contribute to our sweat rate measurements.

2.3. Characterization of Fluidic Microchannel

The fluidic microchannel is an improved version of our previous study.[35,36] Sweat rate measurements from the electrical admittance between two parallel electrodes spiraling within the microchannel suffer from selectivity limitations as the admittance is impacted by the changing ionic composition of accumulating sweat. Nevertheless, the discrete output of alternating comb-like electrodes presented in the previous study can be blurred if the sweat does not take on a plug-like flow (sudden step increase in the admittance magnitude) profile through the microchannel. However, the face-to-face electrodes in this work show a robustly discrete step in admittance upon the crossing of each electrode gate, enabling direct quantification of the flow rate as shown in **Figure 3**a. It is important to note that the absolute magnitude change in the admittance value does not have any effect on the sweat rate monitoring as we only count the number of gates crossed within a certain time period. The number of gates crossed can be detected from the sudden step in the magnitude without requiring the actual admittance change value.

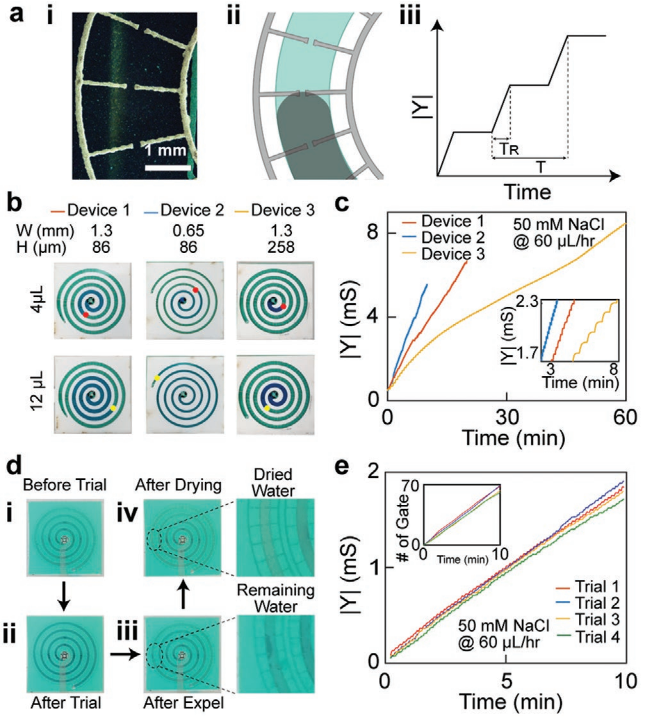

Figure 3. Electrical characterization of the fluidic microchannel. a) Geometry of the face-to-face comb-like electrode—optical image (i), schematic drawing showing fluid flow in the channel (ii), step in the admittance response where time *T* is the total time to cross a gate and *Tr* is the rise time (time required to pass the electrode from the touching of the electrode) (iii). b) Optical photographs of three different devices with varying channel widths and heights. The red circle marked the liquid front in the channel for 4 μL fluid while the yellow circle marked the liquid front for 12 μL fluid. c) Measured admittance of three devices shown in (b), inset is the zoomed admittance to depict the steps in the admittance measurement due to the electrode gate crossing of the fluid. d) Process of resetting the device for multiple uses. e) Admittance measurement of three trials of one device, inset is to show the similar number of gate crossing within same time while the actual admittance change can be different.

The detection capability of absorbent pad-based sweat rate monitoring devices[29,30,41] depends on the evaporation rate of the wicking/absorbent pad, thus dependent on the environmental humidity and temperature. In contrast, one of the main restricting factors of the fluidic microchannel is that the admittance-based sweat rate measurement can only continue if there is empty volume available along the microchannel so that the accumulating sweat in the collection well can advance into the channel and increase the admittance. We have studied three devices with different widths and heights but with a constant length of 189 mm (Figure 3b) to show the tunability of the volume capacity of the fluidic channel. For uniform fluid flow in the channel, the sidewalls were treated with hydroxyl group silane (protocol is described in the Experimental Section), which made it hydrophilic.[42] Synthetic sweat (50×10^{-3} M NaCl) is delivered into the device with an injection pump at a constant rate of 60 µL h^{-1}, which is in the range of the healthy subject's sweat rate. Optical photographs were taken to visualize the liquid front at two different liquid volumes in the channel. The red circle shows the liquid front at 4 µL and the yellow circle shows the liquid front at 12 µL (Figure 3b). The electrical admittance measurements are operated at 1 MHz using a benchtop LCR meter so that the measured admittance is in a simple relation with fluid volume (Figure 3c). With a 1.3 mm width and 0.086 mm height, the volume capacity of Device 1 is 21 µL, whereas the volume capacity of Device 2, with a width of 0.65 mm and height of 0.086 mm, is 10.5 µL. As the channel width decreases, the sensitivity of the channel increases, since the sweat front moves faster through the channel, decreasing the time between each electrode gate crossing. On the other hand, the height of Device 3 is increased to three times that of Device 1, while keeping the width and length the same. The volume capacity of Device 3 is increased to 63 µL, while the sensitivity decreases, as more fluid is needed to cross the gates, and hence the detection time increases. It is interesting to note that for Device 3, the measured admittance is not linear for a full range; the capacitive gates are in parallel connection with two spiraling electrodes, so the more gates covered by the fluid the more parasitic capacitance comes into effect. However, this does not affect the sweat rate monitoring as absolute magnitude changes are not required.

Then, we studied the capabilities of our device during repeated trials to check whether these devices can be used multiple times, which is a limiting factor for many of the adhesive-based microfluidic devices, as they are designed to be single-use and disposable. The resetting process of a microfluidic channel has been studied in our previous publication.[36] Figure 3d shows the fluidic channel after each step during the resetting: i) before the first trial, ii) after the first trial when the device is completely full, iii) after expelling the liquid by using a negative pressure suction cup and an absorbing pad, and iv) after drying the device. Four repeated admittance measurements shown in Figure 3e confirm the reusability of these fluidic layers with overall acceptable sweat rate tracking capability. When performing this trial, inconsistent flow rates have been noticed when using the micropump equipment.

2.4. Digital On-Body Sweat Rate Monitoring

Next, we tested our device on a human subject to monitor continuous real-time sweat rate as shown in **Figure 4**ai. The device was placed on the forearm of a healthy volunteer, along with continuous-monitoring sensors for heart rate on the wrist and a CORE Temperature sensor under the arm. Sweat rate, core body temperature, skin temperature, and heart rate were simultaneously measured (Figure 4b). The subject was instructed to bike for 30 min and then rest for 10 min. For a moderate biking speed of 14 mph, the time elapsed from the start of pedaling to the start of sweat rate measurements is about 14 min for this device. This includes the time for the onset of sweating after starting exercise as well as the time for sweat to fill the device collection well and inlet, which make up its dead volume. Once sweat reaches the device microchannel, sweat rate measurements can begin. The dyed sweat can be visually monitored as it flows in the channel to optically determine the collected sweat volume (Figure 4aii). This scheme for optical sweat rate tracking is realized via discrete photographs of sweat progression (every minute) within the channel.

The continuous admittance measurement was done using an LCR meter (Figure 4biv). The discrete admittance changes, or steps, occur when sweat accumulating and advancing in the channel bridges the gap between protruding electrode spokes, forming a sudden additional electrical connection between the two electrode backbones and creating an overall admittance signal that uniquely depends on the position of the sweat front within the channel. As the spacing between the spokes is known and the channel cross-section is fixed, each time the sensor signal undergoes a discrete step change we can determine how much additional volume of fluid was added to the channel. The volume resolution of the device with a cross-section of 0.086 mm × 1.3 mm, and electrode spokes situated at 1.27 mm intervals is 142 nL. Increasing the number of radial electrodes allows for higher temporal resolution of sweat rate measurements if needed. The electrical sweat volume and sweat rate measurement are then compared to optical sweat volume and sweat rate measurement and were found to be within 1–2 gate crossings of each other (Figure 4bv,vi). Figure 4bii,iii shows that the heart rate and underarm skin temperature profiles are also aligned with the sweat rate profile, with the rise in heart rate and skin temperature at the start of cycling soon followed by the onset of sweating, and the end of cycling followed by a drop in the heart rate, sweat rate, and skin temperature, in that order.

2.5. Simultaneous Local Sweat Rate Monitoring from Multiple Locations

Continuous tracking of sweat secretion can help uncover valuable insights into personal health, especially for athletes who need to maintain proper fluid and electrolyte balance. We tested the capabilities of our sweat collection device in monitoring sweat rate at different locations on the body. We placed seven devices on various skin sites, specifically the forehead, left and right biceps, left and right forearm, and left and right ankle to fully investigate the sweat secretion profile as shown in **Figure 5**a. A sensor for core body temperature was also worn under the clothes in the underarm area. The volunteer subject was asked to bike at different speeds. Colored dye was used to visualize the sweat progression in the fluidic channel and optical images were taken periodically as displayed in Figure 5b. All the devices were of the same collection area size to demonstrate the variation in secretion rate immediately after capturing the optical image.

Figure 5c shows the sweat gland densities obtained by a bromophenol blue dye method. The body sites were spotted with bromophenol dye (preparation process is discussed in the Experimental Section) to directly color the sweat glands. After applying a thin layer of dye on the skin, the subject was asked to bike for a few minutes and the activated sweat glands were visible in the optical image as blue-colored pores. The number of glands was counted in a large area, with a ruler scale at

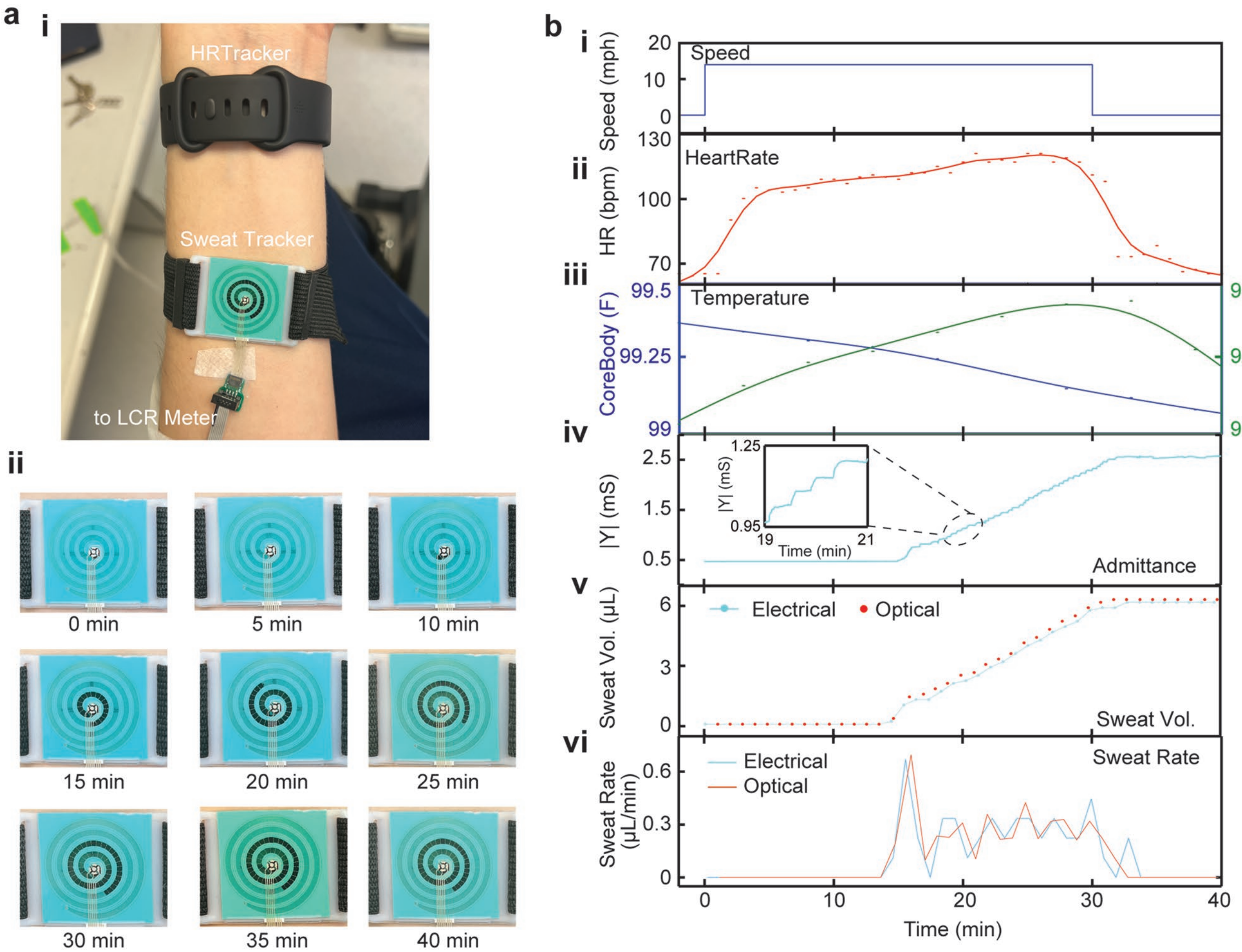

Figure 4. Real-time continuous sweat rate monitoring. a) Optical image of a subject wearing a tape-free digital sweat rate monitoring device along with a heart rate (HR) monitoring device on the wrist (i). A CORE temperature sensor was placed in the underarm area. Periodical optical images of the sweat rate device for visual monitoring of the sweat front colored with the dye (ii). b) Simultaneous monitoring of biking speed (i), measured heart rate (ii), core body and skin temperature (iii), electrical admittance reading of the sweat rate device (iv), comparison of electrically and optically collected sweat volume (v), and comparison of electrically and optically monitored sweat rate (vi).

the side, and the density was calculated per cm^{-2}. The results reveal that the forehead and forearm have higher sweat gland densities than the bicep and ankle (the ankle had the lowest at the site of testing). The sweat rate is dependent on the active sweat glands' size and densities rather than total density. The substantially higher and similar active sweat gland densities on the forehead and forearm surfaces suggest the sweat rate from these should be similar with slight variation due to the elasticity of the underlying skin (elasticity of the skin defines the dead volume of the device as skin bulged into the curved collection well).[38,43] Although the distribution of sweat glands is not uniform across the whole body, the left and right test sites have similar active sweat gland density, supporting the potential use of the device on only either side of the body to predict full body sweat profile without loss of information.

As the subject was biking at a moderate speed of 15 mph, sweat quickly began to accumulate in the collection well, driven by the secretion pressure of the glands, and entered the channel within a few minutes. For a sweat rate of ≈350 nL min^{-1} cm^{-2} in the forehead and forearm, it takes ≈7 min to fill the dead volume of the device (≈2.8 μL for a device with a 1.144 cm^2 collection area), matching the earlier analysis of the device's dead volume optimization in Figure 2b. The sweat onset in the channel of the devices in both left and right forearm also coheres with the similar active sweat gland distribution in this area. Devices on the biceps started to fill in the channel in 10 min at a sweat rate of ≈200 nL min^{-1} cm^{-2}, indicating that the experimental dead volume is lower than the calculated dead volume in Figure 2b. This may be due to the higher skin deformation in the soft bicep area than in the forearm area used in the calculation for analysis in Figure 2. While devices on the bicep started to fill at around 10 min, the ankle with lower sweat gland density started later. The discrepancy between the start times of the right and left ankles (13 and 19 min, respectively) could arise from imperfect device placement, resulting in the sourcing of differing sweat gland densities or sizes, and poor sealing due to body hair. The core body temperature depicts the internal body thermoregulatory physiology of the subject as the muscle produces heat during

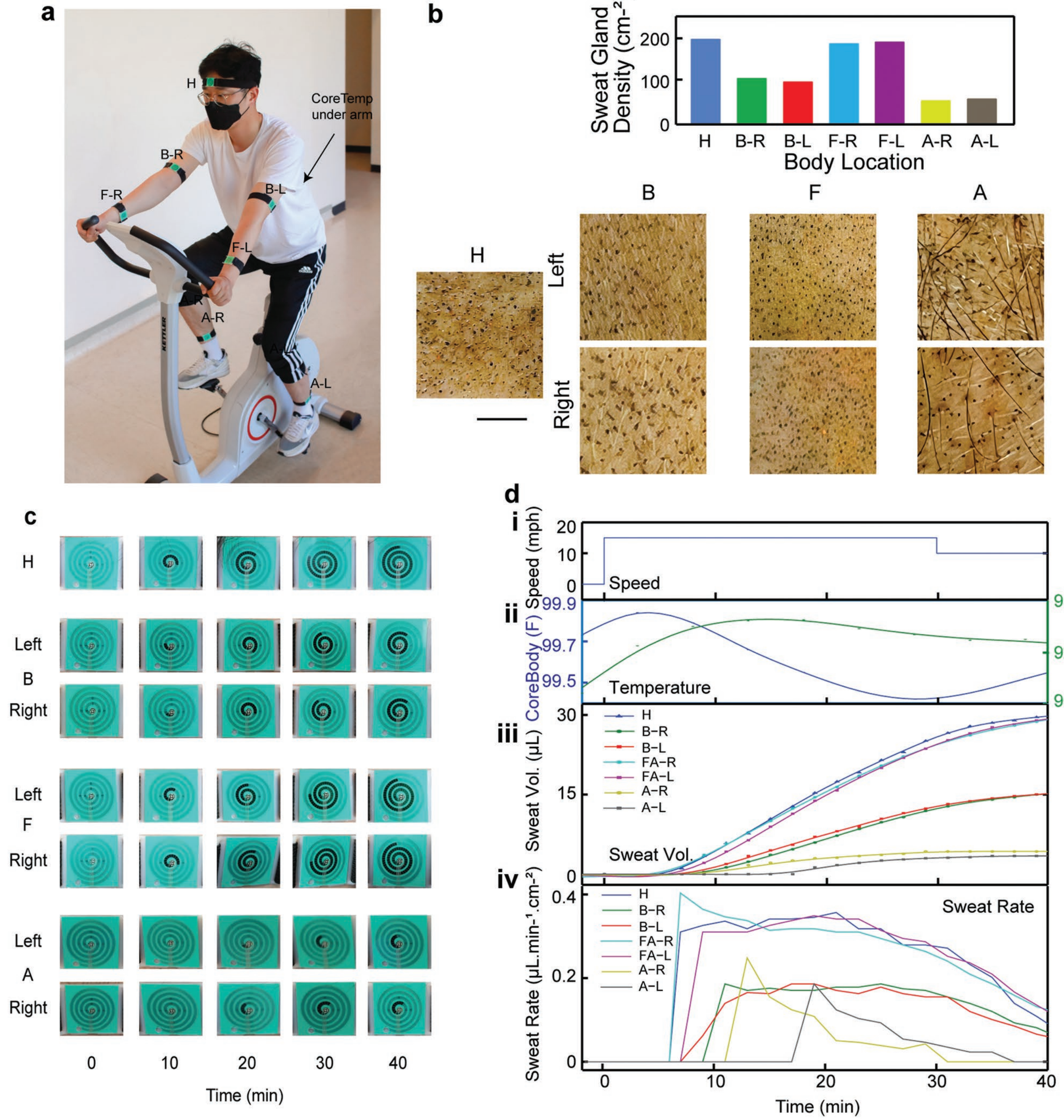

Figure 5. Simultaneous regional sweat rate monitoring from multiple body locations. a) Placement of seven sweat rate monitoring devices on the forehead (H), both left and right forearms (F), biceps (B), and ankles (A), and a CORE Temperature device in the underarm area. b) Optical images and sweat gland densities in the seven body locations mentioned in (a). c) Periodical optical photographs of the devices worn at various locations to visualize the sweat front over time. d) Simultaneous monitoring of biking speed (i), core body and skin temperature (ii), collected sweat volume from seven locations (iii), and four-point simple moving average of the sweat rate at seven locations (iv). Scale bar is 5 mm.

the exercise. With an initial increase in the body temperature, the temperature then decreases once the subject sweats at a higher rate and increases again during the slow biking period.[28,30] On the other hand, the skin temperature increases initially due to the warming up of the body, and then becomes steady, as the subject starts sweating, until the end of the trial, as the skin temperature is ideally the temperature of the secreted sweat.

2.6. Multi-subject and Longitudinal Sweat Rate Studies

As sweat rate profiles at each body position vary across subjects, further on-body trials were performed in order to gauge the consistency of the sweat rate measurements across different subjects. We asked four volunteers to partake in our cycling experiment, a 60-min trial of continuous biking at a constant and comfortable speed. Each volunteer repeated this experiment three to four times at the same speed. With minimal irritation seen across our experiments, the Agilus30 material proved to be safe and comfortable. If worn for longer periods of time, such as 6 h with increased tightness, it may leave a small mark on the skin that goes away with time. In order to assess the relationship between a subject's sweat rate at various body positions, we defined two continuous metrics: 1) fill volume ratio and 2) sweat rate ratio. The fill volume ratio is defined as the ratio between the total amount of sweat accumulated in two different body positions at a given time. For this study, we primarily looked at the ratios between the forehead and bicep (H/B), the forehead and forearm (H/F), and the bicep and forearm (B/F). It is important to compare the ratios between a subject's positional sweat volumes because they account for the natural differences in a subject's sweat gland composition. The continuous plot of this ratio, as illustrated in **Figure 6**a–d, shows a general trend of convergence from around the halfway mark. So, while some sensors may fill up faster than others depending on the subject, the ratio between such positional accumulations serves as a benchmark expectation for the subject's sweat profile. Furthermore, we defined the sweat rate ratio as the ratio between the sweat rates at two different positions. The continuous sweat rate for each position was computed by dividing the change in fill volume by the change in time for each overlapping four-sample window in our dataset. By using a rolling average approach, we reduced human measurement errors without oversimplifying our dataset. Figure 6a illustrates this continuous ratio side-by-side with the fill volume ratio. As fluctuations are expected due to the granularity of our measurements, the ratios tend to remain proximal, indicating that different sensors' flow rates perform consistently throughout each experiment.

Moreover, while the continuous fill volume and sweat rate ratios help monitor device performance during the trial, a new discrete metric was introduced to assess the consistency of the sensors across various trials for the same subject: net sweat rate ratio. The net sweat rate ratio compares the net sweat rates between two different positions. For each position, the net sweat rate is computed by dividing the total fill volume of each sensor at the end of the experiment by the time since the sensor began to fill. The net sweat rate ratio is then computed by taking the ratio of the two positions' net sweat rates. This metric offers insight into a sensor's overall sweat rate performance during a trial. Figure 6e,f illustrates the net sweat rate ratios for H/B, H/F, and B/F across multiple trials for each subject. We found that the relationship between a subject's bicep and forearm (B/F) net sweat rates tended to perform most consistently across trials; however, we observed that each subject had one trial where their forehead's net sweat rate significantly exceeded that of their biceps and forearms. In order to account for this variability, the median is used to capture the benchmark ratios for each subject. As more trials are performed, we expect this benchmark to become even more indicative of a subject's natural sweat rate profile, and it not only will be used as a verification tool for our sensor's performance, but a subject's deviation from this benchmark may provide a proactive approach to detecting signs of hyperhidrosis.

Finally, while the sweat rates of subjects are partially dependent on the ambient climate, the sensor's performance was not noticeably affected during these trials with varying ambient weather conditions such as high humidity (tests

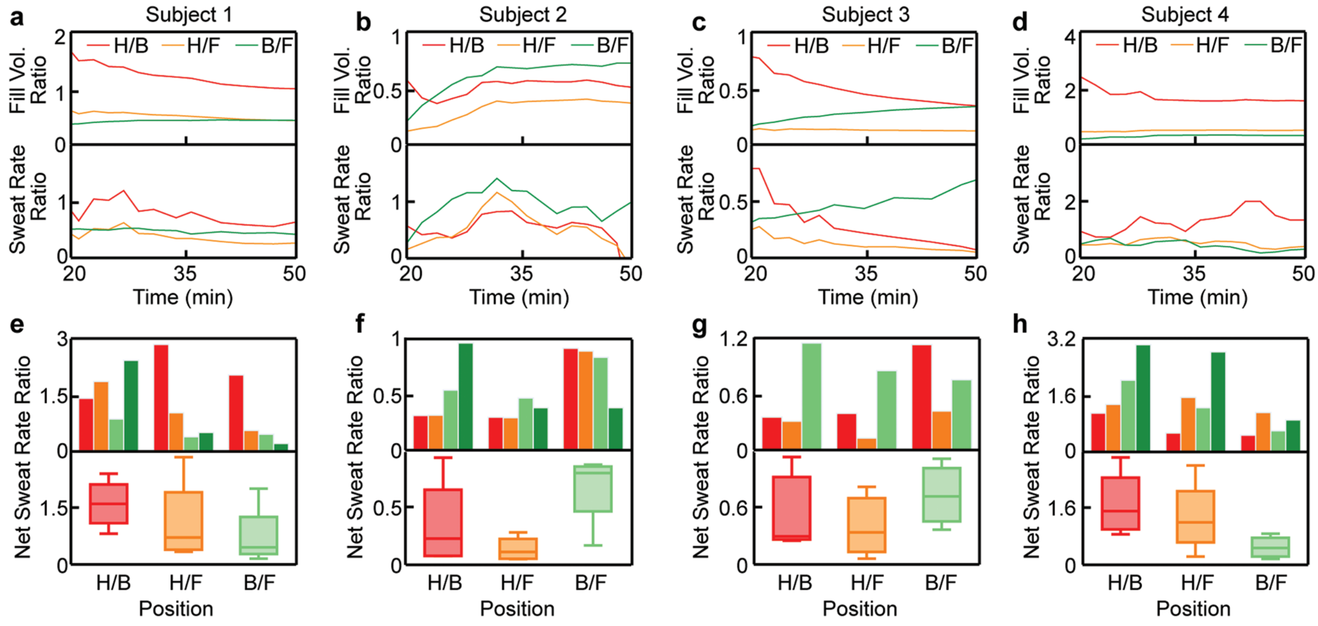

Figure 6. Multi-subject and longitudinal sweat rate studies. a–d) Instantaneous fill volume and sweat rate ratio at different locations for subjects 1 through 4. For instance, fill volume ratio H/B refers to the ratio between the sweat fill volume in the forehead and the sweat fill volume in the bicep at a given time during the trial. e–h) Net sweat rate ratio at different locations for longitudinal studies for subjects 1 through 4 (experiments were performed independently for each subject, and sweat rates were monitored at different body locations). For instance, net sweat rate ratio H/B refers to the ratio between total sweat fill volume divided by the total time the sensor began accumulating sweat in the forehead and bicep. Detailed statistical methods are included in the Experimental Section.

performed at 20%–82% relative humidity) and temperature (tests performed at 20–37 °C). Environmental humidity significantly affects sweat evaporation on the skin, however, the evaporation inside the microfluidic channel is small due to the small cross-sectional area between the liquid front and the environment. In addition, further isolation tests were conducted to demonstrate the sensor's performance in high-temperature and high-humidity environments (Figure S3, Supporting Information).

2.7. Correlation between Local Sweat Volume and Total Fluid Loss

Maintaining fluid balance is essential for healthy vital functions. This is especially relevant in athletics, where proper fluid replacement during practice and competition is critical for ensuring physical and mental well-being.[12,13,26] As sweating correlates with whole-body fluid loss and is the primary source of electrolyte excretion during exercise, sweat testing can be used to monitor fluid imbalances. To understand the relationship between local sweat volume and whole-body fluid losses, we performed 15 cycling trials ranging from 40 to 60 min in duration. We then plotted the sweat volume at each location against the total fluid loss exhibited by the subject directly after the experiment (**Figure 7**a–d). After plotting the line of best fit and calculating the R-coefficient for each position, it was determined that the bicep and ankle's sweat volumes correlated well with a subject's fluid loss (Figure 7b,d), while the forearm and forehead correlated the least (Figure 7a,c). The demonstrated sweat rate profile at different locations and their correlation with total fluid loss can be used to design a single device to study the full-body sweat dynamics. For example, rather than using multiple devices to collect sweat from the whole body (similar to the whole-body wash-down method), we would be able to use one single device to monitor sweat rate at a local body location to predict the total fluid loss. While future work may entail adding more variables to the linear regression (e.g., trial temperature or humidity), these preliminary findings indicate that fluid loss for controlled exercises may be predictable from a subject's bicep and ankle sweat profiles.

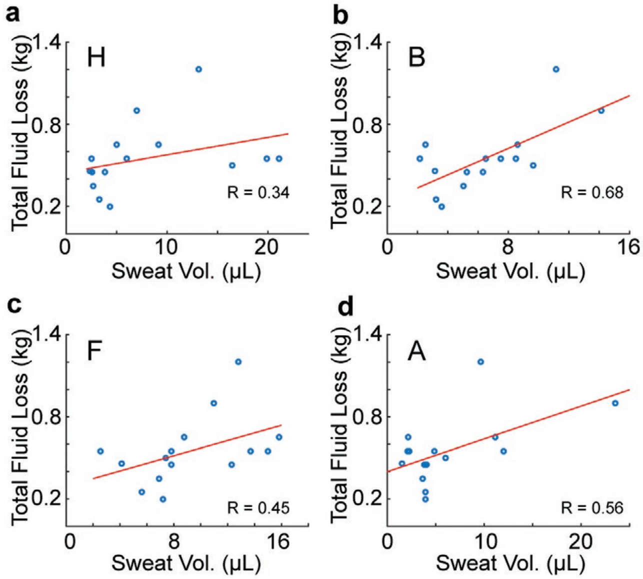

Figure 7. a–d) Correlation between total fluid loss and local sweat volume with an R-coefficient of 0.34, 0.68, 0.45, and 0.56 for H, B, F, and A, respectively. Sweat volumes collected from left and right sides were averaged to present only B, F, and A.

The measurement of regional sweat rate can be of high importance in analyzing the correlation between the secretion rate at different body locations. As this tape-free device encapsulates sweat immediately and uses a narrow channel to create a rapid movement of the sweat front, translating into frequent and live sweat rate measurements. This device would not only overcome the leakage problem associated with many recent sweat rate devices but it can also be integrated with existing wearable devices for continuous health and fitness tracking.

3. Conclusion

A common form factor for wearable sweat rate monitoring devices is a patch format, which uses tape to interface the skin. In this work, we present smartwatch-compatible sweat rate monitoring, which utilizes a tape-free 3D printed sweat collector that is designed to maintain an air-free watertight seal against the skin. The soft and flexible material used to fabricate the sweat collector well provides a smooth interface for comfortable long-time wear of the device. In addition, the device's layered design lends itself to further experimentation with the sweat collector's geometry and microfluidic volume capacity to further enhance the device's sweat-collecting capabilities at different body locations. Furthermore, the impedimetric sensing enables continuous digital monitoring of the sweat rate for prolonged multi-subject and longitudinal studies, which provides insight into the regional sweat profile and its correlation with total fluid loss. Future works will include the addition of electrochemical sensors in the fluidic channel for total sweat composition analysis with the same device and existing methods. Wireless portable electronics are to be developed for remote monitoring of health status, integrated with available products such as a smartwatch or fitness tracker. We envision this device potentially being used in monitoring sweat dynamics for personalized health and fitness monitoring.

4. Experimental Section

Fabrication of Fluidic Microchannel: The detailed fabrication process of the fluidic microchannel was included in a previous study.[35,36] In brief, a roll of polyethylene terephthalate (PET) substrate (DuPont Teijin Films Melinex ST506, 125 µm thick) was thermally pretreated (oven at 140 °C, 5 m min^{-1}, dwell time ≈ 0.7 min) before sequential roll-to-roll rotary silk screen printing of i) silver conductive tracks (Asahi LS-411AW, oven-dried at 140 °C, 2 m min^{-1}, drying time ≈ 3 min), ii) carbon electrodes (Loctite EDAG PF-407A, oven-dried at 140 °C, 4 m min^{-1}, drying time ≈ 2.1 min), iii) two dielectric layers (Loctite EDAG 452SS, UV-cured, 4 m min^{-1}), and iv) upper silver electrodes (Asahi LS-411AW, oven-dried at 140 °C, 2 m min^{-1}, drying time ≈ 3 min). Printed layers were manually registered, with the alignment monitored using a camera module mounted on the printing line. Laser (ELAS laser system with Ekspla Atlantic DPL 015 3 laser head employing 355 nm wavelength. SCANLAB IntelliSCAN III 14 galvanometer deflection unit with F-theta objective of 330 mm and scan head controlled by a SCANLAB RTC5 control board) patterned electrode sheets, channel-defining double-sided microfluidic adhesive tape (3 M 9965), and polyester cover film (3 M 9984) were manually assembled to form the microfluidic sensing patch.

Silanization: For uniform fluid flow, the sidewalls of the laser-cut channel were functionalized with a hydrophilic hydroxyl-silane.[42] The channel was first treated with O_2 plasma (30 W, 0.2 mTorr) for 2 min. Next, it was infiltrated in 0.25 wt% N,N-bis(2-hydroxyethyl-3-aminopropyl)-triethoxysilane, HEA (Gelest, Inc.) in anhydrous ethanol (>99.5%, Sigma-Aldrich) for 5 min, followed by a thorough rinse with anhydrous ethanol. Finally, the layer was dried with N_2 followed by completed dry at 60 °C for 20 min.

Fabrication of Sweat Collector: The sweat collector has two parts: 1) a 2:1 mixture of RGD531 and RGD515 digital ABS-based hard housing and 2) Agilus30 Clear-based flexible collection well. It was printed by using an Objet260 3D printer that prints layer by layer on a soluble support material (FullCure SUP706). After printing the sweat collector, a water jet was used to clean the support material and a 1 mm diameter needle was used to clean the inlet hole. Isopropanol alcohol was used to clean the inlet hole afterward. Finally, a double-sided tape (3 M 1577) was used to attach the fluidic microchannel to the sweat collector. A Velcro with two strap bands was used to wear the device on the body. Moreover, Figure S1 (Supporting Information) provides a comprehensive comparison of this device's geometry and dimensions compared to other sweat rate sensors found in literature.

Device Characterization: To measure the dead volume of the sweat collector, dye-colored liquid was flown by using a 1 mL syringe (BD Plastic) with a 16-gauge flat needle while the sweat collector was worn by a subject using a Velcro and the amount of liquid needed to fill the collection well was measured. The measurements were repeated 5 times for sweat collectors of varying collection well size and curvature. To investigate the leakage, two experiments were performed, a) the collection well was colored with the dye, and b) a 1 cm hole was filled with colored dye. In both cases, the sweat collector was worn for 6 h, and photographs were taken before and after wearing the sweat collector to check visually whether any liquid leaks into the outer mark of the sweat collector.

For electrical characterization, a controlled flow rate was maintained using Harvard Apparatus PHD 2000 Syringe Pump. A 1 mL syringe with a 16-gauge needle was used, and the needle was inserted into the inlet hole of the sweat collector. Electrical admittance was measured using E4980AL precision LCR meter (Keysight Technologies).

On-Body Sweat Analysis: In addition to the sweat rate monitoring device, for heart rate measurements, a Fitbit wristwatch fitness tracker (Fitbit Charge 3) was used, and for temperature monitoring, a CORE Temperature Device was used. For the stationary bike trial, the subject cycled on an electronically braked leg-cycle ergometer (Gold's Gym Cycle Trainer 290C). A scale was used to measure the total nude body weight before and immediately after the bike trials.

For electrical sweat volume measurement, admittance steps representing face-to-face comb-like electrode gate crossings were converted to collected sweat volume by utilizing a custom algorithm that fits a piecewise constant function to the admittance data.[44] By specifying constraints for what constitutes a "step" in the admittance plot, the algorithm counts the number of steps in each minute interval, representing the number of gates that the sweat in the microfluidic has covered per minute. The cumulative sweat volume and the sweat flow rate were then calculated by multiplying the number of gate crossings in each minute by 142 nL, the resolution of each gate. This algorithmic process is outlined in Figure S2 (Supporting Information). For optical sweat volume measurement, colored dye (food color) was used to visually track the sweat front in the fluidic microchannel. Photographs were taken every 2 min and the number of gate crossings was identified to measure the collected sweat volume. Then, a four-point simple moving average of the derivative of the fill volume was taken for the sweat rate profile.

For Sweat gland analysis, Bromophenol Blue (BMB) dye method was used. First, the BMB was mixed in acetone at a 1:5 (w/v) ratio. Then silicone (Corning DowSil 342) was added to this mixture at a 1:1 (v/v) ratio and stirred on a hot plate at 25 °C using a magnetic stirring bar until the acetone evaporated away. A thin layer was then applied to the skin and the subject was asked to bike for 5–10 min and photographs were taken to count the sweat gland density.

Statistical Analysis:

1. For sweat rate calculations: Sweat rate was calculated as the collected sweat volume between two consecutive measurements at any time divided by the time. Then a four-point simple moving average was used to post-process the data.
2. Fill volume ratio: The fill volume ratio is a continuous metric computed by dividing the total fill volume of a sensor at a specific body position by the total fill volume of another at a specific time during a trial. If two sensors were used to capture the sweat volume at a body position (e.g., left and right forearm), the average fill volume between them is used to represent the position's fill volume.
3. Sweat rate ratio: The sweat rate ratio is a continuous metric computed by dividing the sweat rate of a sensor at a specific body position by the sweat rate of another. The sweat rate is computed using a rolling average approach to reduce variance: for a given time t_1, we define $t_2 = t_1 - 8$ min, creating an 8-min window. The change in fill volume within this window was divided by $t_1 - t_2$, yielding the sweat rate for a specific position. Similarly, to the fill volume ratio calculation, if two sensors are used to capture the sweat volume at a body position, the average sweat rate between them is used to represent the position's sweat rate.
4. Net sweat rate ratio: The net sweat rate ratio is computed by dividing the net sweat rate of a sensor at a specific body position by the net sweat rate of another. The net sweat rate is calculated by dividing the total fill volume of a sensor at the end of a trial by the total time the sensor was collecting sweat. So, if sweat began filling at the 10-min mark of a 60-min trial, the net sweat rate is precisely the total fill volume of a sensor at the end of the trial divided by 50 min.

Supporting Information

Supporting Information is available from the Wiley Online Library or from the author.

Acknowledgements

On-body human trials were carried out at the University of California, Berkeley in compliance with the human research protocol (CPHS 2014-08-6636) approved by the Berkeley Institutional Review Board (IRB). Informed consent was obtained from the subjects before enrollment in the study. This work was partially supported by National Science Foundation through grant NASCENT-1160494, and by the Berkeley Sensors and Actuators Center (BSAC) and the Bakar Fellowship. Part of the facilities at VTT was funded by the Academy of Finland Research Infrastructure "Printed Intelligence Infrastructure" (PII-FIRI, Grant No. 320020). Technical assistance from Jari Rekilä (screen printing and laser layout design for fluidic microchannel) and Hannu Sääskilahti (R2R screen printing) is gratefully acknowledged. N.D. acknowledges support from the National Defense Science & Engineering Graduate (NDSEG) Fellowship Program.

Conflict of Interest

The authors declare no conflict of interest.

Author Contributions

M.D. and L.F.A.-C. contributed equally to this work. M.D., L.F.A.-C., N.D., and A.J. conceived the idea and designed the experiments.

M.D. performed the studies with the help of L.F.A.-C. and wrote the manuscript with the help of L.F.A.-C., N.D., A.A., J.P., and S.W. N.D. and L.F.A.-C. designed the devices. L.G., E.J., M.H., and J.H. contributed to the manufacture of the fluidic microchannel with printed electrodes. M.D., A.A., and A.J. performed and interpreted the statistical analysis. All authors discussed the results and revised the manuscript.

Data Availability Statement

The data that support the findings of this study are available from the corresponding author upon reasonable request.

Keywords

3D printed, fluid loss, leakage-free, reusable, sweat rate, tape-free, wearable devices

Received: July 19, 2022
Revised: October 20, 2022
Published online:

---

[1] C. Glaros, D. I. Fotiadis, in *Intelligent Paradigms for Healthcare Enterprises*, Studies in Fuzziness and Soft Computing, Vol. *184* (Eds: G. Silverman, B. Jain, A. Ichalkaranje, A. C. Jain), Springer, Berlin **2005**, pp. 237–264.
[2] A. Mahajan, G. Pottie, W. Kaiser, *ACM Trans. Comput. Healthcare* **2020**, *1*, 3361561.
[3] J. Kim, A. S. Campbell, B. E.-F. de Ávila, J. Wang, *Nat. Biotechnol.* **2019**, *37*, 389.
[4] M. Dautta, M. Alshetaiwi, A. Escobar, F. Torres, N. Bernardo, P. Tseng, *Adv. Electron. Mater.* **2020**, *6*, 1901311.
[5] A. Hajiaghajani, A. H. A. Zargari, M. Dautta, A. Jimenez, F. Kurdahi, P. Tseng, *Nat. Electron.* **2021**, *4*, 808.
[6] J. Kim, E.-F. Chou, J. Le, S. Wong, M. Chu, M. Khine, *Adv. Healthcare Mater.* **2019**, *8*, 1900109.
[7] O.-H. Huttunen, M. H. Behfar, J. Hiitola-Keinänen, J. Hiltunen, *Adv. Mater. Technol.* **2022**, *7*, 2101496.
[8] M. Bariya, H. Y. Y. Nyein, A. Javey, *Nat. Electron.* **2018**, *1*, 160.
[9] M. Chung, G. Fortunato, N. Radacsi, *J. R. Soc., Interface* **2019**, *16*, 20190217.
[10] E. J. M. Moonen, J. R. Haakma, E. Peri, E. Pelssers, M. Mischi, J. M. J. den Toonder, *VIEW* **2020**, *1*, 20200077.
[11] W. P. Cheshire, R. D. Fealey, *Drug Saf.* **2008**, *31*, 109.
[12] B. Nielsen, M. Nielsen, *Acta Physiol. Scand.* **1965**, *64*, 314.
[13] R. A. Oppliger, C. Bartok, *Sports Med.* **2002**, *32*, 959.
[14] L. B. Baker, J. B. Model, K. A. Barnes, M. L. Anderson, S. P. Lee, K. A. Lee, S. D. Brown, A. J. Reimel, T. J. Roberts, R. P. Nuccio, J. L. Bonsignore, C. T. Ungaro, J. M. Carter, W. Li, M. S. Seib, J. T. Reeder, A. J. Aranyosi, J. A. Rogers, R. Ghaffari, *Sci. Adv.* **2020**, *6*, eabe3929.
[15] W. C. Randall, C. N. Peiss, *J. Invest. Dermatol.* **1957**, *28*, 435.
[16] J. Heikenfeld, A. Jajack, B. Feldman, S. W. Granger, S. Gaitonde, G. Begtrup, B. A. Katchman, *Nat. Biotechnol.* **2019**, *37*, 407.
[17] W. Gao, S. Emaminejad, H. Y. Y. Nyein, S. Challa, K. Chen, A. Peck, H. M. Fahad, H. Ota, H. Shiraki, D. Kiriya, D.-H. Lien, G. A. Brooks, R. W. Davis, A. Javey, *Nature* **2016**, *529*, 509.
[18] A. J. Bandodkar, W. J. Jeang, R. Ghaffari, J. A. Rogers, *Annu. Rev. Anal. Chem.* **2019**, *12*, 114910.
[19] Y. Song, J. Min, Y. Yu, H. Wang, Y. Yang, H. Zhang, W. Gao, *Sci. Adv.* **2020**, *6*, eaay9842.
[20] A. Koh, D. Kang, Y. Xue, S. Lee, R. M. Pielak, J. Kim, T. Hwang, S. Min, A. Banks, P. Bastien, M. C. Manco, L. Wang, K. R. Ammann, K.-I. Jang, P. Won, S. Han, R. Ghaffari, U. Paik, M. J. Slepian, G. Balooch, Y. Huang, J. A. A. S. Rogers, *Sci. Transl. Med.* **2016**, *8*, 366ra165.
[21] G. Matzeu, C. Fay, A. Vaillant, S. Coyle, D. A. W. Diamond, *IEEE Trans. Biomed. Eng.* **2016**, *63*, 1672.
[22] K. Chen, J. Ren, C. Chen, W. Xu, S. Zhang, *Nano Today* **2020**, *35*, 100939.
[23] J. Heikenfeld, *Electroanalysis* **2016**, *28*, 1242.
[24] L. B. Baker, *Sports Sci. Exchange* **2016**, *29*, 6.
[25] S. M. Shirreffs, R. J. Maughan, *J. Appl. Physiol.* **1997**, *82*, 336.
[26] L. B. Baker, C. T. Ungaro, B. C. Sopeña, R. P. Nuccio, A. J. Reimel, J. M. Carter, J. R. Stofan, K. A. Barnes, *J. Appl. Physiol.* **2018**, *124*, 1304.
[27] M. U. Parkkinen, R. Kiistala, U. Kiistala, *Arch. Dermatol. Res.* **1991**, *283*, 382.
[28] H. Y. Y. Nyein, L.-C. Tai, Q. P. Ngo, M. Chao, G. B. Zhang, W. Gao, M. Bariya, J. Bullock, H. Kim, H. M. Fahad, A. Javey, *ACS Sens.* **2018**, *3*, 944.
[29] S. Wang, M. Liu, X. Yang, Q. Lu, Z. Xiong, L. Li, H. Zheng, S. Feng, T. Zhang, *Biosens. Bioelectron.* **2022**, *210*, 114351.
[30] H. Liu, H. Qing, Z. Li, Y. L. Han, M. Lin, H. Yang, A. Li, T. J. Lu, F. Li, F. Xu, *Mater. Sci. Eng., R* **2017**, *112*, 1.
[31] J. He, G. Xiao, X. Chen, Y. Qiao, D. Xu, Z. Lu, *RSC Adv.* **2019**, *9*, 23957.
[32] S. Fumarola, R. Allaway, R. Callaghan, M. Collier, F. Downie, J. Geraghty, S. Kiernan, F. Spratt, J. Bianchi, E. Bethell, A. Downe, J. Griffin, M. Hughes, B. King, K. LeBlanc, L. Savine, N. Stubbs, D. Voegeli, *J. Wound Care* **2020**, *29*, S1.
[33] L. McNichol, C. Lund, T. Rosen, M. Gray, *J. Wound Ostomy Continence Nurs.* **2013**, *40*, 365.
[34] F. Tokumura, K. Umekage, M. Sado, S. Otsuka, S. Suda, M. Taniguchi, A. Yamori, A. Nakamura, J. Kawai, K. Oka, *Skin Res. Technol.* **2005**, *11*, 102.
[35] H. Y. Y. Nyein, M. Bariya, L. Kivimäki, S. Uusitalo, T. S. Liaw, E. Jansson, C. H. Ahn, J. A. Hangasky, J. Zhao, Y. Lin, T. Happonen, M. Chao, C. Liedert, Y. Zhao, L.-C. Tai, J. Hiltunen, A. Javey, *Sci. Adv.* **2019**, *5*, eaaw9906.
[36] M. Bariya, N. Davis, L. Gillan, E. Jansson, A. Kokkonen, C. McCaffrey, J. Hiltunen, A. Javey, *ACS Sens.* **2022**, *7*, 1156.
[37] O. Bar-Or, L. I. Magnusson, E. R. Buskirk, *Hum. Biol.* **1968**, *40*, 235.
[38] N. Kondo, M. Shibasaki, K. Aoki, S. Koga, Y. Inoue, C. G. Crandall, *J. Appl. Physiol.* **2001**, *90*, 1877.
[39] K. Sato, F. Sato, *Am. J. Physiol.* **1983**, *245*, R203.
[40] M. Bariya, L. Li, R. Ghattamaneni, C. H. Ahn, H. Y. Y. Nyein, L.-C. Tai, A. Javey, *Sci. Adv.* **2020**, *6*, eabb8308.
[41] G. Havenith, A. Fogarty, R. Bartlett, C. J. Smith, V. Ventenat, *Eur. J. Appl. Physiol.* **2008**, *104*, 245.
[42] R. Yerushalmi, J. C. Ho, Z. A. Jacobson, A. Javey, *Nano Lett.* **2007**, *7*, 2764.
[43] N. A. Taylor, C. A. Machado-Moreira, *Extreme Physiol. Med.* **2013**, *2*, 4.
[44] A. Aggarwal, TapeFreePaper-Algorithms, https://github.com/aaggarw99/TapeFreePaper-Algorithms (accessed: October 2022).